P_n and S_n tomography across Eurasia to improve regional seismic event locations

Michael H. Ritzwoller*, Mikhail P. Barmin, Antonio Villaseñor,
Anatoli L. Levshin, E. Robert Engdahl

Department of Physics, University of Colorado at Boulder, Campus Box 390, Boulder, CO 80309-0390, USA

Abstract

This paper has three motivations: first, to map P_n and S_n velocities beneath most of Eurasia to reveal information on a length scale relevant to regional tectonics, second, to test recently constructed 3-D mantle models and, third, to develop and test a method to produce P_n and S_n travel time correction surfaces which are the 3-D analogue of travel time curves for a 1-D model. Our third motive is inspired by the need to improve regional location capabilities in monitoring nuclear treaties such as the nuclear Comprehensive Test Ban Treaty (CTBT). To a groomed version of the ISC/NEIC data, we apply the tomographic method of Barmin et al. [Pure Appl. Geophys. (2001)], augmented to include station and event corrections and an epicentral distance correction. The P_n and S_n maps are estimated on a $1° \times 1°$ grid throughout Eurasia. We define the phases P_n and S_n as arriving between epicentral distances of $3°$ and $15°$. After selection, the resulting data set consists of about 1,250,000 P_n and 420,000 S_n travel times distributed inhomogeneously across Eurasia. The rms misfit to the entire Eurasian data set from the P_n and S_n model increases nearly linearly with distance and averages about 1.6 s for P_n and 3.2 s for S_n, but is better for events that occurred on several nuclear test sites and for selected high-quality data subsets. The P_n and S_n maps compare favorably with recent 3-D models of P and S in the uppermost mantle and with recently compiled teleseismic station corrections across the region. The most intriguing features on the maps are the low-velocity anomalies that characterize most tectonically deformed regions such as the anomaly across central and southern Asia and the Middle East that extends along a tortuous path from Turkey in the west to Lake Baikal in the east. These anomalies are related to the closing of the Neo-Tethys Ocean and the collision of India with Asia. The uppermost mantle beneath the Pacific Rim back-arc is also very slow, presumably due to upwelling that results from back-arc spreading, as is the Red Sea rift, the Tyrrhenian Sea and other regions undergoing active extension.
© 2002 Elsevier Science B.V. All rights reserved.

Keywords: Eurasia; Upper mantle; Tomography

1. Introduction

Determination of accurate seismic locations and uncertainties is of prime importance in monitoring the

Comprehensive Nuclear Test Ban Treaty (CTBT). Small magnitude events will only be recorded at a sparse subset of the International Monitoring System (IMS) at regional distances less than $20–30°$. Sparse network locations are subject to significant bias due to regional variations in the structure of the crust and upper mantle. To meet the goals of the CTBT for these small events, this bias must be substantially

* Corresponding author. Tel.: +1-303-492-7075; fax: +1-303-492-7935.

E-mail address: ritzwoller@ciei.colorado.edu (M.H. Ritzwoller).

reduced in regions of significant structural variability such as that across much of Eurasia. To do so will require either a model of the 3-D structures themselves or the effects of the structures on the relevant travel times.

This paper has three motivations. The first is to map P_n and S_n velocities beneath most of Eurasia using regional phase data (viz., P_n, S_n) to reveal information on a scale relevant to regional tectonics. The second is to test global (e.g., Ekström and Dziewonski, 1998; Bijwaard et al., 1998; Shapiro et al., 2000) and regional (e.g., Villaseñor et al., 2001) 3-D seismic models. The third and principal motivation is to develop and test a method to produce P_n and S_n Eurasian travel time correction surfaces. These surfaces form a common basis for locating seismic events with regional data alone. Each travel time correction surface is a map centered on a specific seismic station. The value at each point on the map is the travel time observed at the station from a seismic event located at a specified depth. Usually, the predicted travel times are presented relative to the prediction from a 1-D seismic model.

The method to estimate P_n and S_n that we describe here is based heavily on earlier efforts by other researchers (e.g., Hearn et al., 1991). Our method and earlier incarnations suffer from a number of problems. These include the fact that P_n and S_n are not monolithic phases that turn at a uniform depth independent of epicentral distance and tectonic regime, and it is difficult to separate crustal from mantle contributions in the observed travel times. These problems are manifested more strongly on the P_n and S_n maps than on the predicted travel time correction surfaces. Thus, although the methods we employ may not provide ideal means to estimate mantle structures, they suffer far fewer problems in predicting the travel time corrections needed to improve capabilities to locate regional events. The results presented here should, therefore, be seen as a preliminary step toward developing a unified model of the crust and uppermost mantle that results from simultaneous inversion of surface wave dispersion and regional body wave travel times.

In the following, we (1) discuss the data set and the tomographic method, (2) show continental scale images of P_n and S_n variations across Eurasia, (3) display the resulting travel time correction surfaces

for several IMS or surrogate stations, (4) discuss the fit to the regional phase data and inferred uncertainties in the correction surfaces, and (5) briefly discuss some of the velocity anomalies that appear in the P_n and S_n images.

2. Data

P_n and S_n travel times are taken from a groomed version of the ISC and NEIC data bases described, in part, by Engdahl et al. (1998). ISC travel times are for events that occurred from 1964 through 1997 and NEIC data are from 1998 to 1999. The locations of explosions are replaced with "ground truth" locations wherever possible (e.g., Sultanov et al., 1999). We define the phases P_n and S_n as arriving between epicentral distances of $3°$ and $15°$. P_n and S_n may dip into the mantle substantially, particularly beyond epicentral distances of $\sim 8°$. The depth of penetration will depend on the vertical derivative of velocity, which will vary spatially. The truncation of the data set to include rays only if epicentral distances are less than $10–12°$, as in some other studies (e.g., Hearn and James, 1994), would severely restrict path coverage in some areas of Eurasia. To utilize longer paths, it is desirable to correct for the effect of ray penetration into the uppermost mantle. We discuss this correction in Section 3.

This data set consists of 3,672,268 P_n phases and 1,346,676 S_n phases for 5418 stations and 149,929 events worldwide. Data are used in the inversion if the residual relative to the prediction from the 1-D model ak135 (Kennett et al., 1995) is less than 7.5 s for P and 15 s for S, if the event depth is within the crust or less than 50 km deep, if the azimuthal gap to all reporting stations for the event is less than $180°$, and if the nominal error ellipse is less than 1000 km^2 in area. These selection criteria reduce the data set to 1,636,430 P_n and 493,734 S_n phases worldwide. Most of these paths cross Eurasia ($0–80°$N latitude and $-10°$W–$180°$E longitude plus a buffer zone), the numbers being 1,257,052 for P_n and 422,634 for S_n. Data density is shown in Fig. 1. Because path lengths for these phases are by definition short ($<15°$), paths only exist in regions where both sources and receivers are common. Thus, the path distribution is highly heterogeneous across the region.
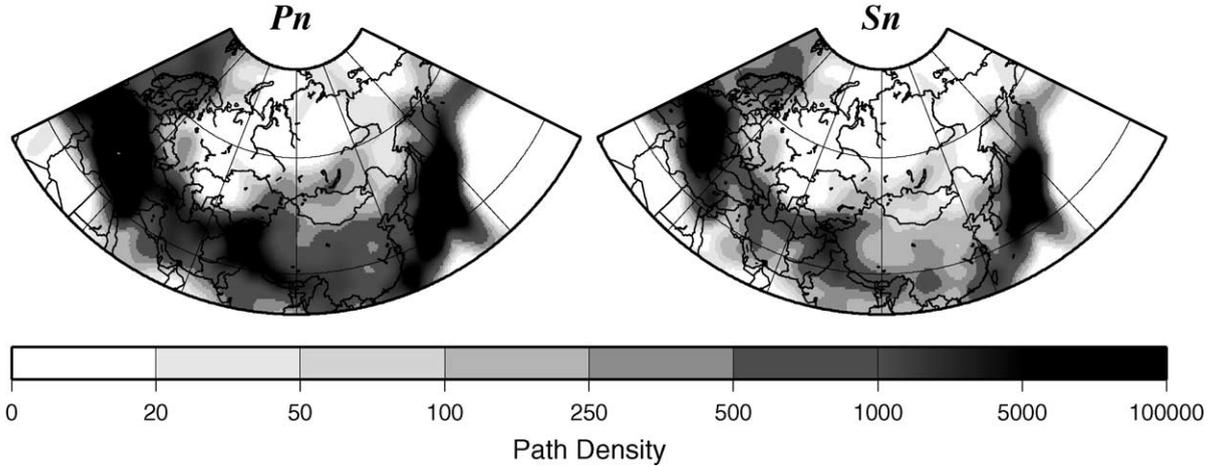
Fig. 1. Path density for the P_n and S_n data, defined as the number of paths intersecting a $2° \times 2°$ cell ($\sim$ 50,000 km^2).

We further reduce this data set by rejecting late arriving travel times at epicentral distances from $3°$ to $6°$ that may be misidentified crustal phases (e.g., P_g) or Moho reflections (PmP, SmS). In addition, in the tomography, we reject measurements misfit by the starting model at more than 2σ, where σ is the average misfit produced by the starting model. This is done to help stabilize the station and event corrections. However, we report misfit statistics relative to the entire data set across Eurasia.

3. Method

The observed travel time, t_{obs}, is modeled as follows:

$$t_{obs} = t_m + t_{crust\_sta} + t_{crust\_evt} + \delta t_{sta} + \delta t_{evt} + \delta t(\Delta) + \delta t_m, \qquad (1)$$

where t_m is the predicted travel time for rays through the mantle part of the input reference model, the contributions to the travel time due to the crustal part of the reference model on the event and station sides are t_{crust_sta} and t_{crust_evt}, the station and event delays or static corrections are δt_{sta} and δt_{evt}, $\delta t(\Delta)$ is the distance correction, δt_m is the travel time correction for the mantle part of the path, and Δ is epicentral distance. Thus, t_m,

t_{crust_sta}, and t_{crust_evt} are predicted by the reference model and δt_{sta}, δt_{evt}, $\delta t(\Delta)$, and δt_m are estimated. If v_m is the velocity along path p in the reference model and δv_m is the model perturbation along the same path, then:

$$t_m = \int_p \frac{ds}{v_m}, \qquad (2)$$

$$\delta t_m = - \int_p \frac{\delta v_m}{v_m^2} ds. \qquad (3)$$

We assume that the ray through the perturbed model, $v_m + \delta v_m$, takes the same path as the ray through the reference model. In practice, we estimate the 2-D quantity δv_m from which we compute δt_m for each ray p.

We use CRUST5.1 (Mooney et al., 1998) as the starting (reference) model in the crust and for mantle P and S. At each geographical point, CRUST5.1 only has one value of P and one value of S for the mantle, intended to characterize the velocity immediately below Moho. Thus, for the reference model, the mantle leg of each path p is horizontal, following directly below Moho as shown in Fig. 2. This is, in fact, a common approximation in P_n and S_n tomography, but realistic rays dive into the mantle to depths that depend on a nonzero vertical velocity derivative as Fig. 3b shows. Fig.
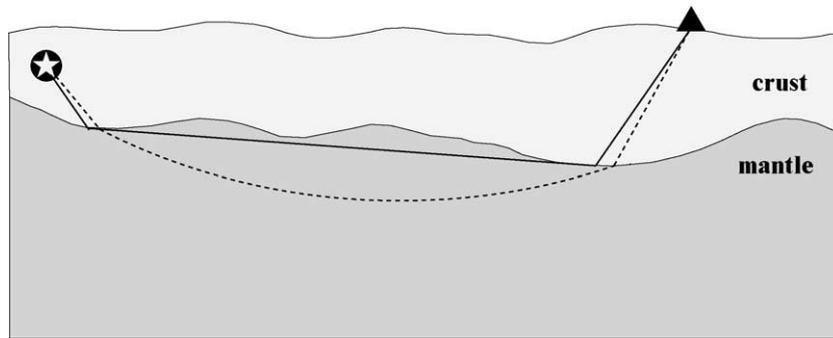
Fig. 2. Illustration of sources of error in the tomography. Real ray paths (dashed line) follow different paths through both the crust and mantle than the hypothesized rays (solid line) used in tomography. In particular, real paths dip deeper into the mantle as epicentral distances increase in a way that depends on the vertical velocity gradient.

3c attempts to quantify the error made by the horizontal ray approximation, by comparing the travel times of rays diving into the mantle through a recent Eurasian 3-D model (Shapiro et al., 2000) with those computed for a model in which the rays propagate horizontally directly beneath Moho. The horizontal ray approximation produces an error that is a relatively smooth function of distance. For most of the continent, the estimated errors are similar and grade smoothly to a travel time error predicted to be about -2.5 s at $15°$ for P velocities. This motivates the introduction into Eq. (1) of a term that is a smooth function of distance, which we call the distance correction, $\delta t(\Delta)$. The correction $\delta t(\Delta)$ attempts to reduce the mantle velocities distributed in 3-D to a single 2-D datum surface which, by design, lies directly below Moho. The paths from WMQ and ANTO in Western China and Turkey, respectively, exhibit anomalously high and low vertical velocity gradients. In these regions, the errors produced by the horizontal ray approximation will be atypical and will be poorly corrected by $\delta t(\Delta)$.

Although the distance correction is an average across the continent, it allows us to fit data over a broader distance range than would be possible without the correction. We find that with this correction, the tomographic maps agree well with those produced with short path data alone (epicentral distances less than $10°$) in those regions where tomographic maps can be constructed reliably using only the short path data. The use of a 3-D model to compute the distance

correction is beyond the scope of the present work, but is an important direction for future research.

We follow Hearn and collaborators (e.g., Hearn and Clayton, 1986; Hearn et al., 1991; Hearn and James, 1994; and elsewhere) and estimate event and station corrections. These corrections are designed to compensate for errors in the reference crustal model, errors in the prediction of the location of the mantle piercing points, and errors in event locations and origin times. A correction is estimated for a station if there are phase picks from at least seven events made at that station and an event correction is estimated for all events for which there are at least 20 reporting stations. The asymmetry in this condition is because there are more physical phenomena modeled with the event correction than with the station correction (e.g., mislocation, origin time error). The station and event corrections are undamped.

As presented here, the P_n and S_n maps are defined over a two-dimensional surface and, therefore, may be estimated with the same 2-D tomographic method we developed for surface wave tomography (Barmin et al., 2001). The inversion for P_n and S_n is approximately the same except that, from the reference model, we compute source and receiver side Moho penetration points and use these points as the starting and ending points of the ray during inversion (see Fig. 2). The approximation comes from the assumption that P_n and S_n rays are "horizontal" in a spherical mantle and propagate directly below Moho, as discussed above and depicted in Fig. 2.
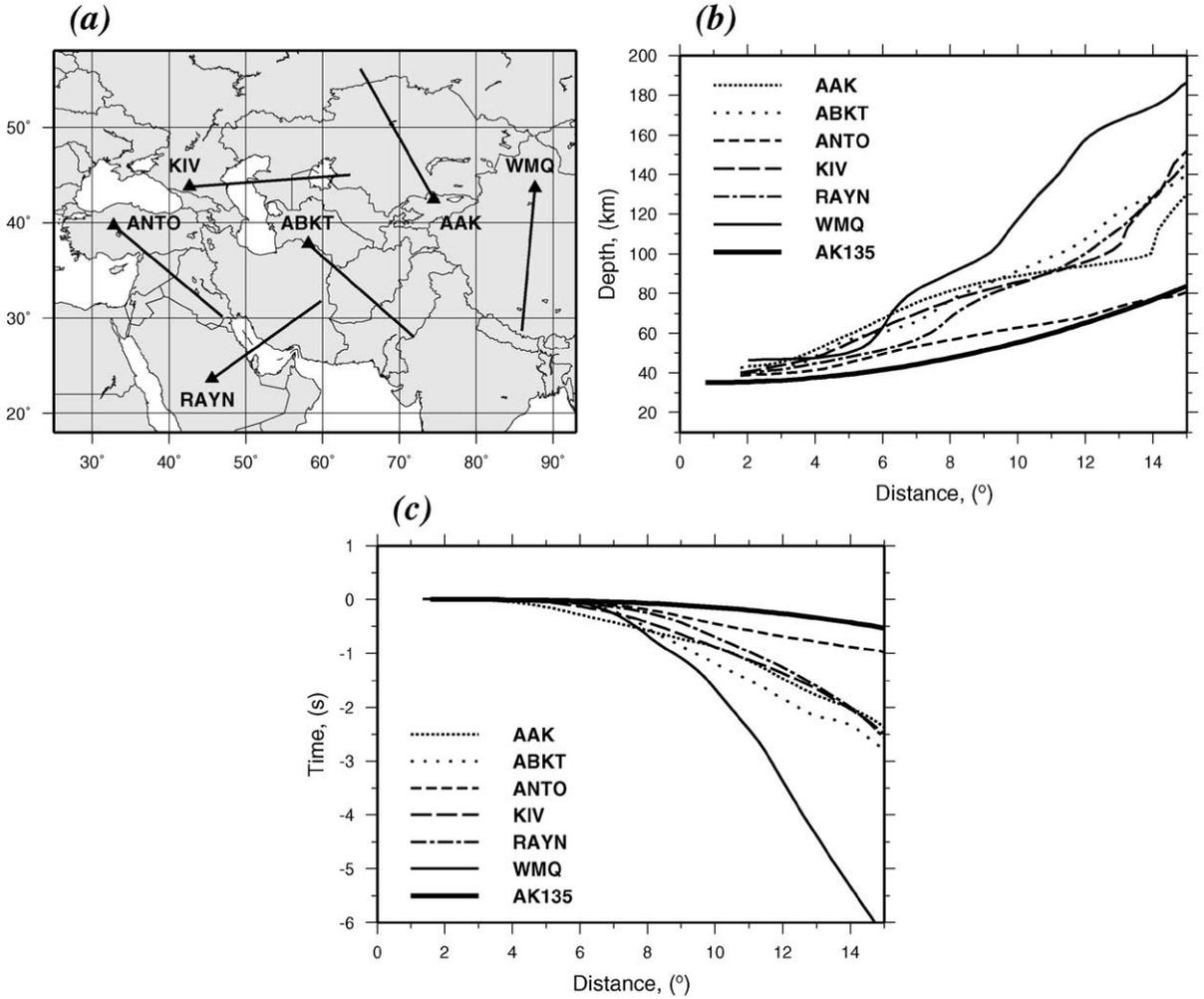
Fig. 3. Examples to justify the distance correction, $\delta t(\Delta)$. (a) The location of the six 2-D velocity profiles used in (b) and (c). Each profile starts from a seismic station and runs for $15°$. The 3-D model used is that of Shapiro et al. (2000). (b) Turning point curves for the six profiles in (a) and for the 1-D model ak135. (c) Each curve is the difference between the travel time travel computed through the 3-D model of Shapiro et al. (2000) using the ray shooting method of Cerveny and Psencik (1988) and the travel time through the same model with a horizontal ray. This provides an estimate of the error in P-wave travel time caused by the horizontal ray approximation for the six profiles in (a).

In the method of Barmin et al. (2001), the model is constructed on an equally spaced grid such that the following figure-of-merit is minimized:

$$(\mathbf{Gm} - \mathbf{d})^{\mathrm{T}} \mathbf{C}^{-1} (\mathbf{Gm} - \mathbf{d}) + \sum_{k=0}^{n} \alpha_k^2 \, \| F_k(\mathbf{m}) \|^2$$

$$+ \sum_{k=0}^{n} \beta_k^2 \, \| H_k(\mathbf{m}) \|^2, \tag{4}$$

which is a linear combination of data misfit, model roughness, and the amplitude of the perturbation to a reference model. The vector $\mathbf{m}$ represents the estimated model, δv_{m}, which is a perturbation relative to a reference across the region of interest, $\mathbf{G}$ is the forward operator that computes travel time from the estimated model, $\mathbf{d}$ is the data vector, $\mathbf{C}$ is the data covariance matrix or matrix of data weights, F is a Gaussian smoothing operator, and H is an operator that penalizes the norm of the model $\mathbf{m}$ in regions of

poor data coverage. The spatial smoothing operator is defined over the 2-D model as follows:

$$F_k(\mathbf{m}) = m_k(\mathbf{r}) - \int_S S_k(\mathbf{r}, \mathbf{r}') m_k(\mathbf{r}') \mathrm{d}\mathbf{r}', \qquad (5)$$

where S_k is a smoothing kernel:

$$S_k(\mathbf{r}, \mathbf{r}') = K_{0k} \exp\left(-\frac{|\mathbf{r} - \mathbf{r}'|^2}{2\sigma_k^2}\right) \qquad (6)$$

$$\int_S S_k(\mathbf{r}, \mathbf{r}') \mathrm{d}\mathbf{r}' = 1, \qquad (7)$$

and σ_k is the spatial smoothing width or correlation length. The minimization of the expression in Eq. (5) explicitly ensures that the estimated model approximates a smoothed version of the model. The maps are estimated on a $1° \times 1°$ grid across Eurasia with $\sigma_k = 150$ km.

We refer to the P_n and S_n maps together with the parametric corrections δt_{sta}, δt_{evt}, and $\delta t(\delta)$ as the CU P_n/S_n model to distinguish it from our recent 3-D models (e.g., Shapiro et al., 2000; Villaseñor et al., 2001). To compute travel time correction surfaces, the distance correction, the station delays, and the P_n or S_n map must be used.

The method of Barmin et al. (2001) allows us to estimate 2ψ and 4ψ azimuthal anisotropy simultaneously with isotropic P_n and S_n. We find, however, that the estimates of azimuthal anisotropy are not robust with respect to data subsetting and variations in damping. In addition, the joint inversion for isotropic and anisotropic structures dominantly affects only the amplitudes of the isotropic maps, but no more so than the choice of isotropic damping which is itself largely arbitrary. Consequently, we report only isotropic P_n and S_n maps here and safely can ignore the effects of azimuthal anisotropy on these estimates.

4. P_n and S_n tomography

We estimate station delays δt_{sta}, event delays δt_{evt}, the distance correction curve $\delta t(\Delta)$, and the 2-D tomographic quantity $\delta v_{\mathrm{m}}(\theta, \varphi)$ which represents lateral variations in seismic velocities in the uppermost mantle. Latitude and longitude are θ and φ, respectively. There are strong and, essentially, unresolvable trade-offs between subsets of these quantities. For example, a constant velocity shift in the uppermost mantle could be fit either by a constant shift in δv_{m} or by introducing a linear trend in $\delta t(\Delta)$. The station delays, δt_{sta}, also strongly trade-off with δv_{m} directly beneath the station and the value of the distance correction at an epicentral distance of $3°$. The estimated values depend strongly on the inversion algorithm and the order in which the corrections are estimated, if the process is iterative rather than simultaneous. If the process were simultaneous, then values would depend on the relative weights assigned to each correction. We constrain $\delta t(\Delta)$ to be approximately zero at $3°$ and let the curve $\delta t(\Delta)$ have only a moderate negative slope. Thus, we choose to fit much of the signal with station delays and allow a substantial constant shift in δv_{m}.

The magnitudes of station and event delays, δ_{sta} and δ_{evt}, are summarized in Fig. 4. Not surprisingly, the S_n corrections are typically larger than those for P_n, presumably because S variations in the crust and upper mantle are typically larger than P by about a factor of two. The P_n and S_n station delays are geographically coherent and correlate with one another with a poorly determined S/P ratio of about 1.8 relative to the mean of each distribution. Fig. 5 shows that if two stations are closer than 50 km apart, the standard deviation of their station delay is about 0.6 s for P_n and 1.5 s for S_n. Part of this difference is structural, as differences in the station corrections grow with the separation between the stations. Stations and events are not uniformly distributed over the continent, with stations predominantly in stable continental regions and events in tectonically deformed regions. For this reason, together with the fact that the delays are taken relative to a model, the delays are not expected to be zero-mean and, in fact, display a positive mean for the stations and a negative mean for the events.

Although we estimate P_n corrections only for about 60% of the stations and half of the events worldwide and for S_n the numbers are about 50% and 25%, respectively, the great majority of the measurements emanate from events and are recorded at stations that have corrections. This is particularly true for P_n, where only about 3% of
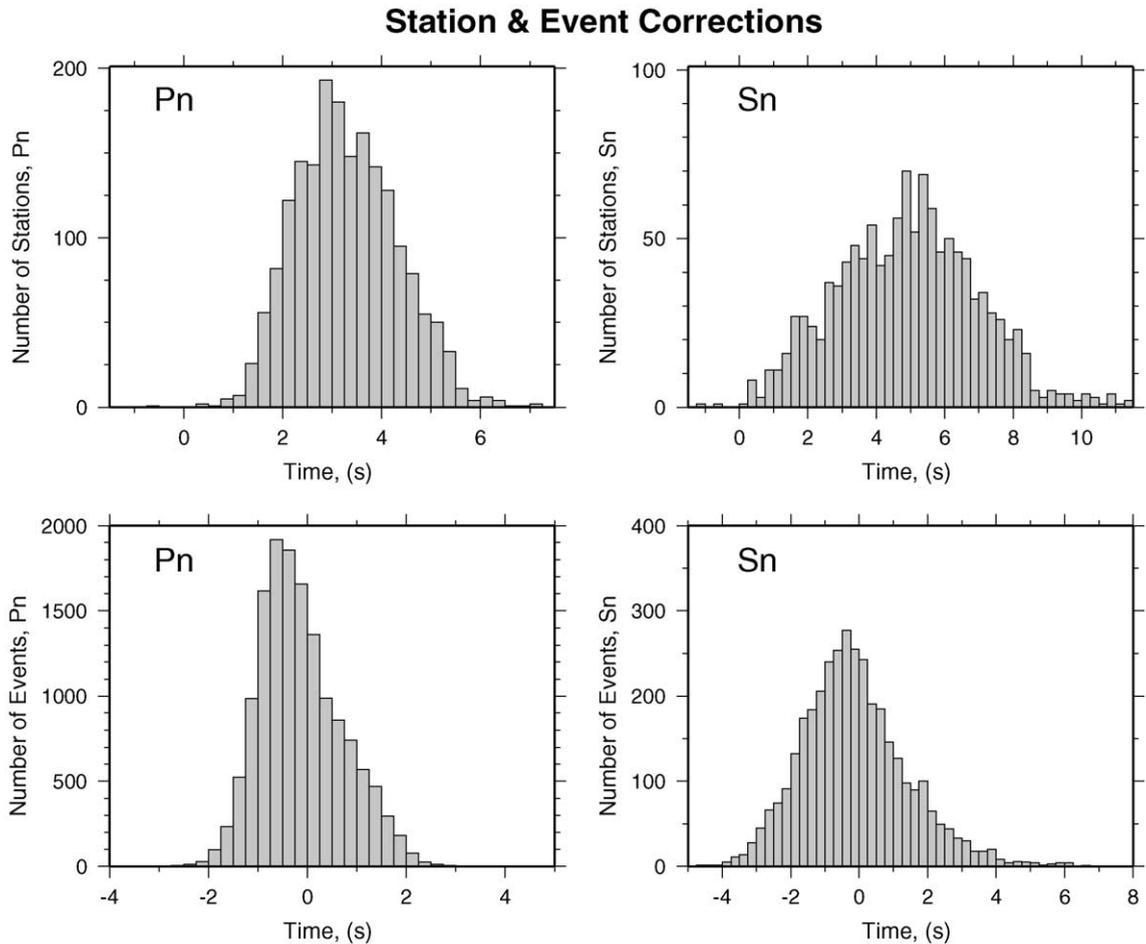
Station & Event Corrections

Fig. 4. P_n and S_n station (top row) and event (bottom row) corrections: histograms of values.

the measurements are made at stations without corrections and 12% are for events without event corrections. For S_n, the numbers are 4% and 33%, respectively. Thus, most measurements have the full complement of corrections applied. For stations and events for which we have not estimated corrections, we set the corrections equal to the mean of the distributions shown in Fig. 4.

The distance correction is shown in Fig. 6. The shape of the P distance correction is different from that predicted by Fig. 3, but the value of the correction at $15°$ is about the same (~ -2.5 s). There is, in addition, a constant offset in δv_m equal to about -100 m/s relative to the average S_n velocity of

CRUST5.1. We have greater confidence in the decisions we reached to resolve the trade-off between δv_m and $\delta t(\Delta)$ for P than for S.

The estimated P_n and S_n maps are shown in Fig. 7. Because our tomographic method penalizes the amplitude of the maps in regions of poor data coverage and the estimated maps are perturbations to a reference state, the maps revert to the reference model where data coverage is poor; i.e., less than $15-20$ paths for each $2° \times 2°$ cell. The areas of poor data coverage are identified as white regions in Fig. 7. Both the P_n and S_n maps demonstrate poor coverage across the shield and platform regions of northern Russia and Kazakhstan, in the oceans, and across North Africa. Elsewhere,
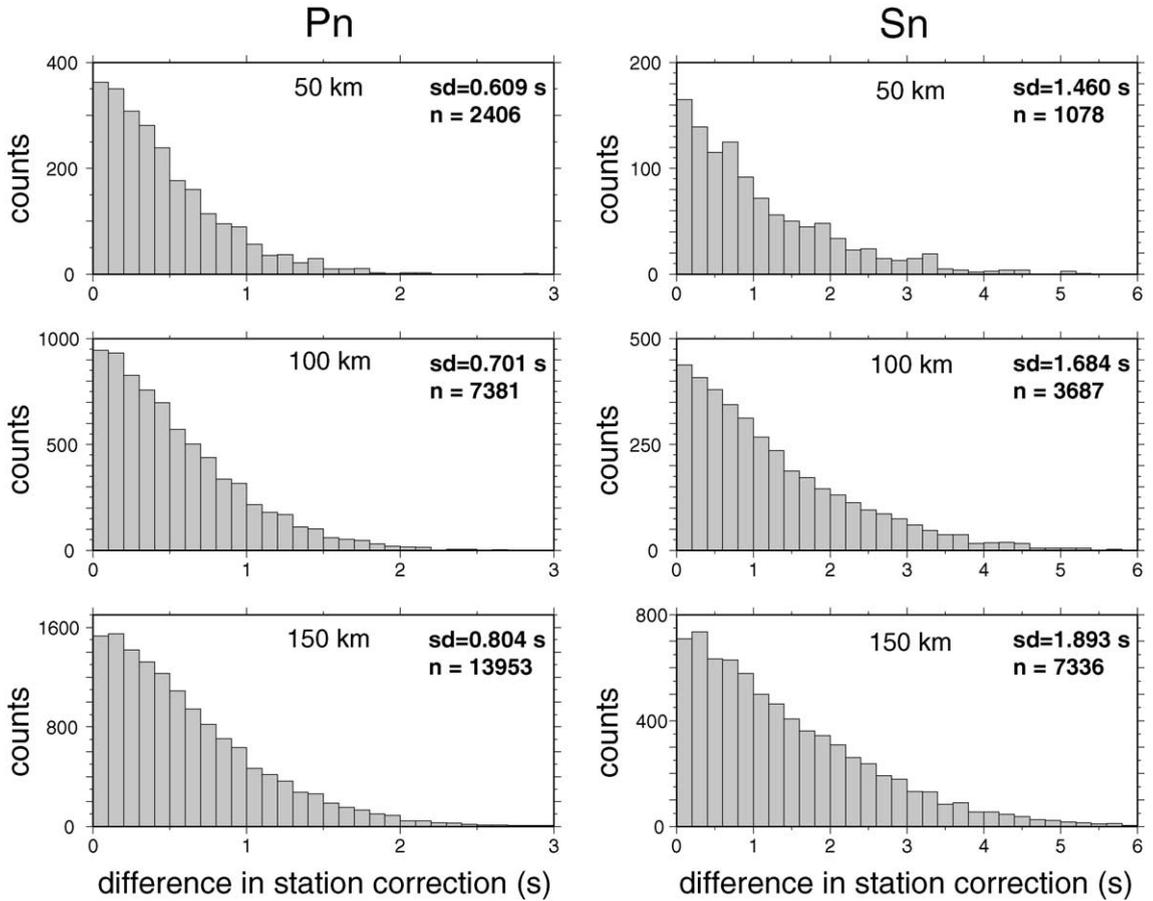
Fig. 5. Spatial coherence of station corrections. Each plot shows the distribution of the absolute value of the difference between the station corrections for nearby stations. In the upper row, the pair of stations lies within 50 km of one another, 100 km in the middle row, and 150 km in the bottom row. Results for P_n are in the left column and for S_n in the right column. The standard deviation (S.D.) of each distribution is marked on each plot as is the number of station pairs (n).

the spatial resolution of the maps is estimated to be between 150 and 300 km.

The P_n and S_n anomalies in Fig. 7 are highly correlated and differ in amplitude by about a factor of two, such that $\delta v_s/v_s \sim 2\delta v_p/v_p$. The anomalies also compare well with known tectonic features and with the patterns of velocity variations at the top of the upper mantle in the $2° \times 2°$ 3-D shear velocity model of Villaseñor et al. (2001). Smaller scale features, however, are apparent in the P_n and S_n maps presented here and the amplitudes of the S_n map are somewhat larger than in the 3-D S model. Villaseñor et al. (2001) also show that the anomalies are similar to those in the teleseismic P model

of Bijwaard et al. (1998) and Engdahl and Ritzwoller (2001) demonstrate that the anomalies correlate with teleseismic station corrections. Thus, the patterns of high and low velocities are robust and are apparent in a number of different data sets at both regional and global scales.

A thorny problem arises in comparing model predictions; namely, the transversely isotropic nature of S models in the upper mantle. Regional S is a split phase and it is unclear if, on average, the observed travel times correspond to SH, SV or some linear combination. We show in Fig. 7 an "equivalent isotropic" shear velocity computed from our 3-D S model, which is approximately the average of v_{sh}
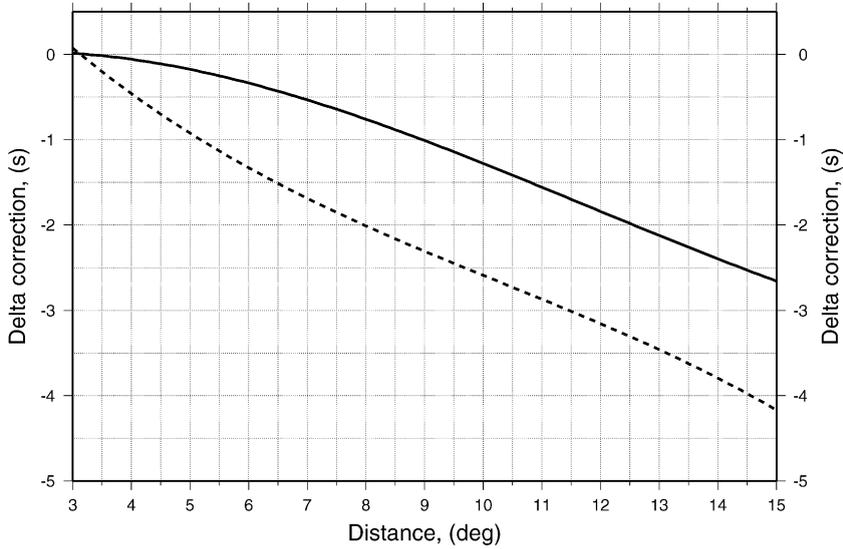
Fig. 6. Estimated distance correction, $\delta t(\Delta)$, for P_n (solid line) and S_n (dashed line). The distance corrections are constrained to be approximately zero at an epicentral distance of 3°.

and v_{sv}. Any offset between the predictions from this S model and the estimated S_n map may result from anisotropy or from improperly resolving the trade-off between the distance correction and δv_{m}, as discussed above. Therefore, it may be most reasonable to compare variations around a poorly determined mean, although Villaseñor et al. (2001) show that inhomogeneities in v_{sh} and v_{sv} in the upper mantle are not correlated everywhere.

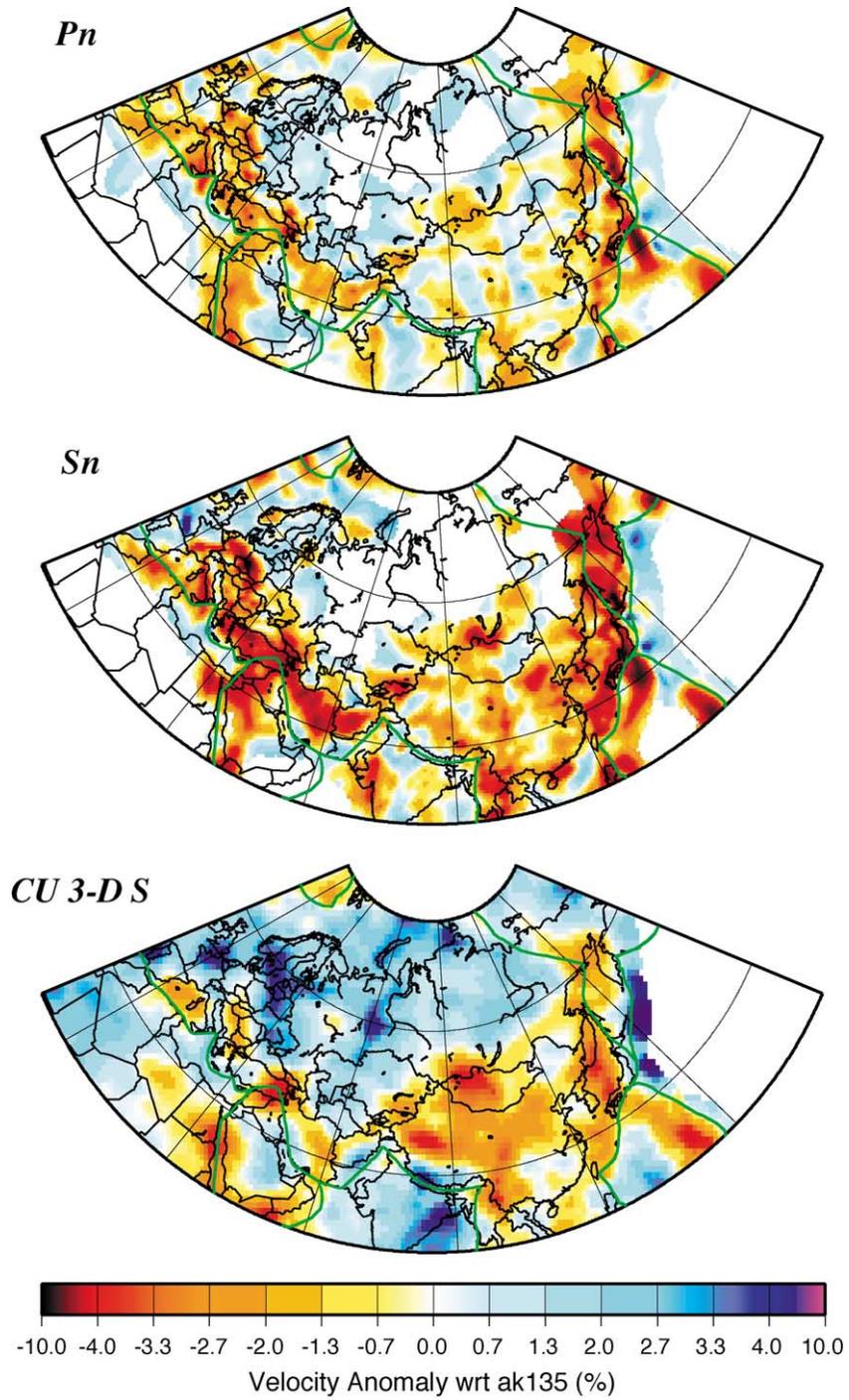## 5. Travel time correction surfaces

Travel time correction surfaces are a computational convenience commonly used for locating seismic events with regional data alone. Each correction surface is a map centered on a specific seismic station. The value at each point on the map is the travel time predicted at the station from a seismic event at a specified depth. They are, therefore, the analogue for a 3-D model of travel time curves for 1-D models. Usually, the predicted travel times are presented relative to the prediction from a 1-D seismic model. The accuracy of regional event locations will depend directly on the accuracy of the correction surfaces.

Using Eqs. (1)–(3) and the notation defined in Section 3, we define the travel time correction surface as follows:

$$
\begin{aligned}
t_{\mathrm{TTCS}}(\Delta, \phi) = {} & t_{\mathrm{m}}(\Delta, \phi) + t_{\mathrm{crust\_sta}}(\Delta, \phi) \\
& + t_{\mathrm{crust\_evt}}(\Delta, \phi) + \delta t_{\mathrm{sta}} + \delta t_{\mathrm{evt}} \\
& + \delta t(\Delta) + \delta t_{\mathrm{m}}(\Delta, \phi) - t_{\mathrm{1D}}(\Delta), \qquad (8)
\end{aligned}
$$

where Δ and ϕ are distance and azimuth from the station to the event, respectively. The prediction from a 1-D model, $t_{\mathrm{1\text{-}D}}$, is subtracted so that the correction surface provides a residual relative to this reference.

Fig. 8 displays travel time correction surfaces for several IMS stations or surrogates. These surfaces are for P_n with surface sources and the station set at the local elevation. This differs from correction surfaces as they are commonly displayed in which both the source and station are on the reference ellipsoid. The peak-to-peak anomaly is about 6 s on each and is typically twice this value for the S_n correction surface. The correction surface for ANTO (Ankara, Turkey) compares favorably with those for two nearby stations in Turkey (KAS, KVT) reported by Myers and Schultz (2000) using a different method.
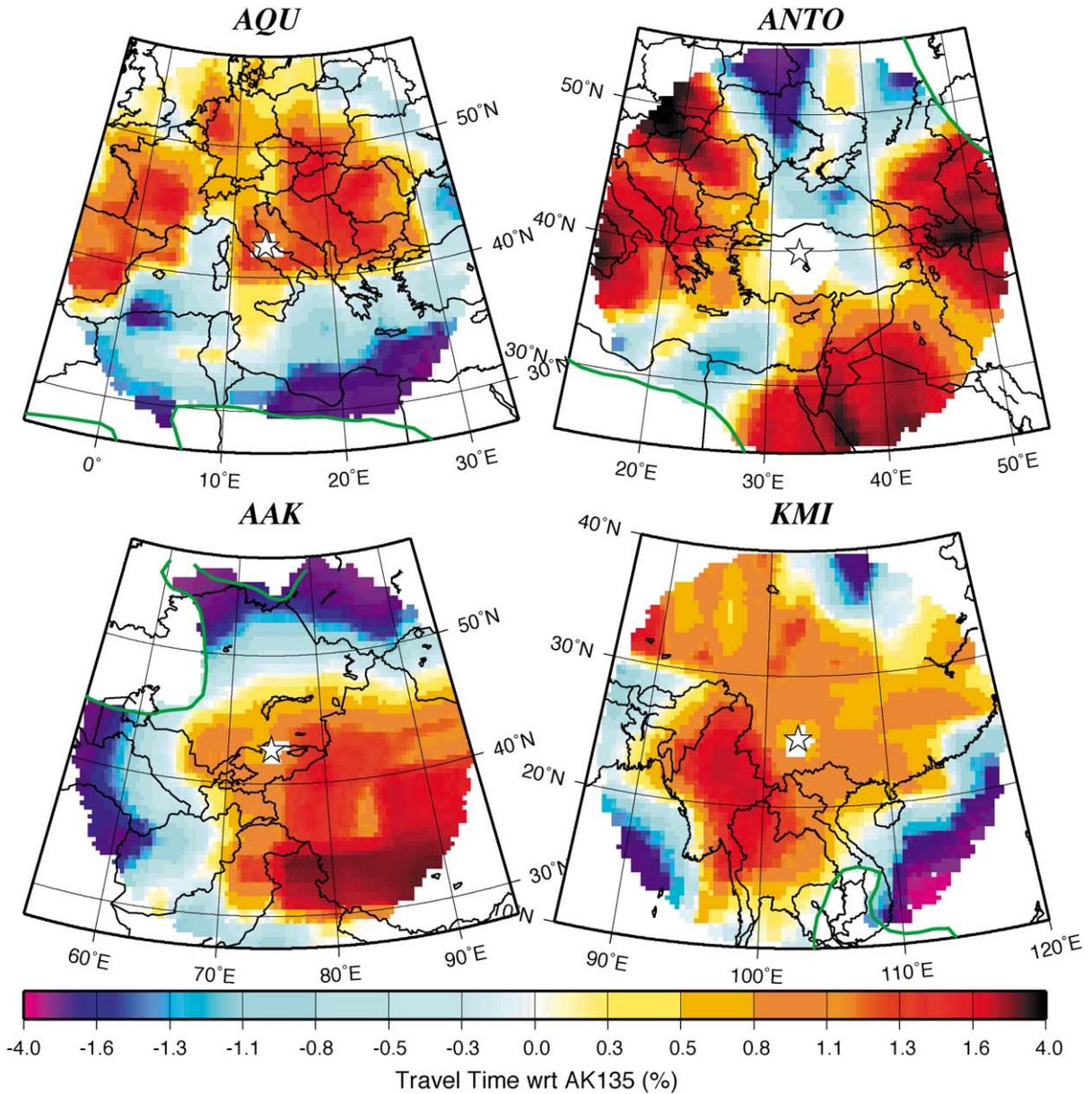
Velocity Anomaly wrt ak135 (%)

Fig. 8. Travel time correction surfaces for P_n for four IMS stations or surrogates identified with stars (AQU, L'Aquila Italy; ANTO, Ankara Turkey; AAK, Ala-Archa Kyrghyzstan; KMI, Kunming China). These surfaces exist only where P_n data density is locally greater than 20 paths/ 50,000 km^2, marked by the green contour, and to 15° from the station. Low data density regions are shaded white. The blocky features that appear in the AAK surface are remnants of the 5° × 5° starting model CRUST5.1.

Fig. 7. P_n and S_n maps estimated across Eurasia. Values are relative to the prediction from ak135 at the top of the mantle, 8.04 km/s for P_n and 4.48 km/s for S_n. The bottom map is the equivalent isotropic S velocity at the top of the mantle from a recently estimated model beneath Eurasia (e.g., Villaseñor et al., 2001). Regions in which path density is less than about 20 paths/50,000 km^2 are poorly constrained by the data, and these regions are shaded white.

Extending correction surfaces beyond 15° will require using a 3-D model to compute the distance correction or the use of 3-D tomography.

6. Evaluation of the results

Misfits to the entire Eurasian data set for P_n and S_n are shown in Fig. 9. Overall summary statistics are presented in Table 1 and rms misfit versus distance is summarized in Fig. 10. The standard

deviation σ reported in Table 1 is computed relative to the distance-dependent mean, so that it represents the scatter around a trend. In general, short distance vertical offsets in Figs. 9 and 10 result in part from errors in the crustal model, either in average crustal velocities or Moho depths. Errors in the uppermost mantle velocities and vertical velocity gradients manifest themselves as trends with distance. The 1-D model ak135 does very well for P. Improvements afforded by the CU P_n/S_n model over ak135 are largest at epicentral distances greater than about
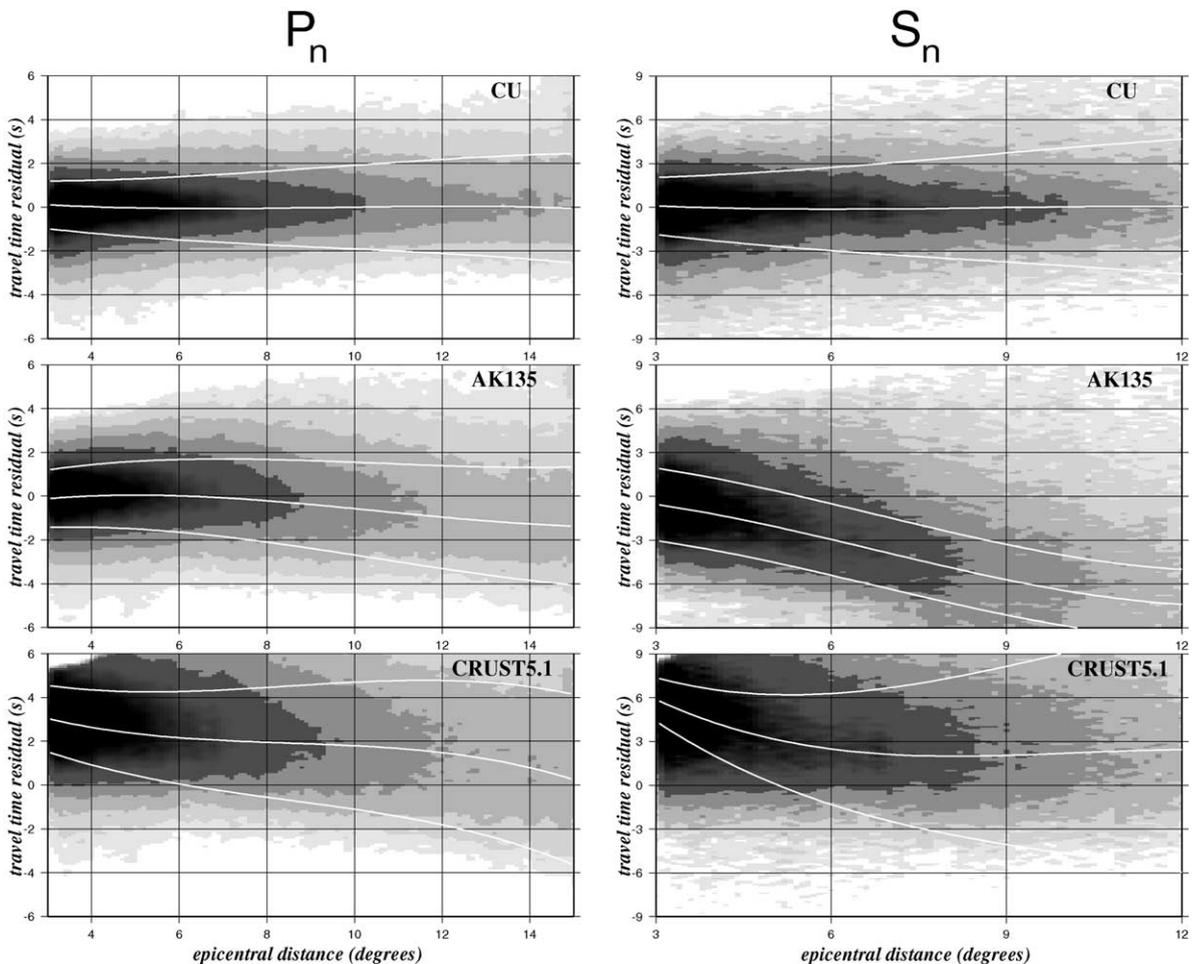

Fig. 9. Shaded plots of the P_n and S_n travel time residuals (observed–predicted) for the Eurasian data set presented versus epicentral distance. Results for three models are shown: (top) the CU P_n/S_n model, (middle) the 1-D model ak135 (Kennett et al., 1995), and (bottom) the laterally heterogeneous crustal, P_n, and S_n model CRUST5.1 (Mooney et al., 1998). Darker shades indicate a larger number of residuals and the white lines show the smoothed local mean and $\pm 1\sigma$. Overall means and standard deviations are summarized in Table 1 and distance trends are shown in Fig. 10.

Table 1
Summary of misfits to the whole Eurasian data set displayed in Fig. 9

Model	P_n		S_n	
	Mean (s)	σ (s)	Mean (s)	σ (s)
CU P_n/S_n	0.01	1.63	0.03	3.20
ak135	− 0.01	1.88	− 2.21	4.29
CRUST5.1	2.51	2.14	4.26	4.25

8°. S misfits from ak135, however, exhibit a strong distance trend, presumably because it is vertically nearly constant from Moho to about 200 km. Thus, the misfit trend in S for ak135 probably results from an error in the vertical gradient in the uppermost mantle. For both P and S, CRUST5.1 is too slow in the crust and S is on average too fast in the uppermost mantle.

The overall rms misfit for the CU P_n/S_n is 1.6 s across all of Eurasia for P_n and approximately twice this value for S_n. These misfit statistics appear to be consistent with those reported by Myers and Schultz (2000) in a study limited to the neighborhood of the 1991 Racha, Georgia earthquake sequence.

The entire Eurasian data set is very noisy and many locations and origin times are poorly known. A better estimate of misfit derived from the errors in the model may come from explosion data in which the epicenter is well constrained in some cases, although the origin times may not be. Fig. 11 displays misfits to data from six explosion regions (three test sites, two Peaceful Nuclear Explosions (PNEs), and one large mining district) and Table 2 summarizes these data. Only explosions with $m_b \geq 4.6$ as reported in the PDE catalogue are used. With the exception of a large mining explosion in southwestern Poland, these events are not observed at enough stations with regional phases to have individually constrained event delays. The overall misfit of the CU P_n/S_n model to these explosion data is 1.68 s for P_n, which is essentially the same as the entire Eurasian data set. For events at the three test sites, however, misfit is better than 1.45 s for P and the fit afforded by ak135 is considerably worse. Again, most of the improvement over ak135 delivered by the CU P_n/S_n model comes for paths longer than about 8°. A similar rms misfit of 1.5 s results

from a subset of the complete Eurasian data set that consists only of events with $m_b \geq 4.6$ and measurements from events with an event correction measured at stations with a station correction. If we remove measurements that fit the reference model (CRUST5.1) beyond the 2σ level, where σ is the standard deviation of misfit for the reference model, we find the overall rms misfit for P_n is about 1.4 s and misfit for S_n is about 2.8 s.
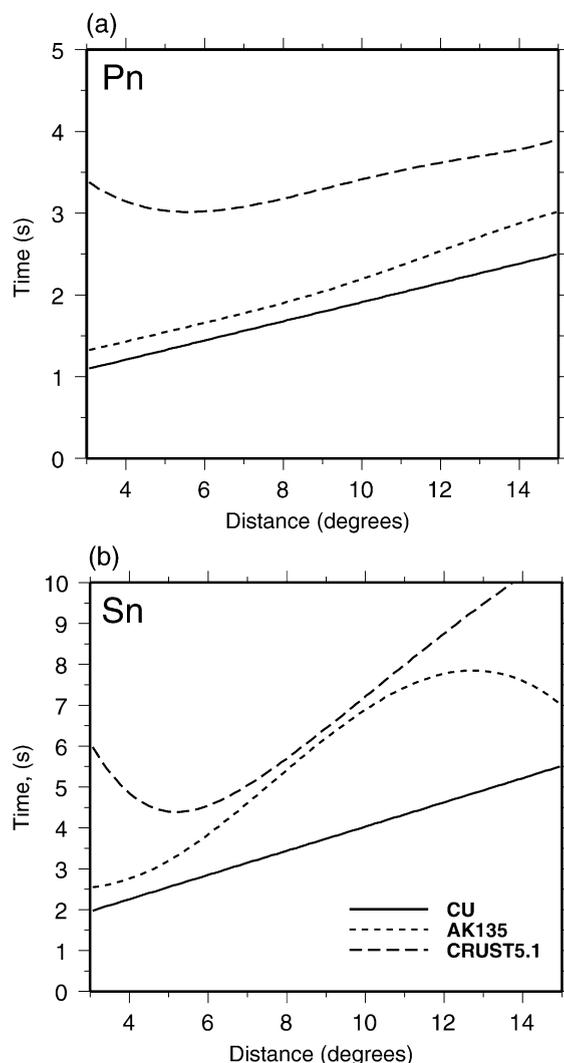

Fig. 10. Smoothed rms misfit versus distance. The solid line is for the CU P_n/S_n model, the dotted line is for the 1-D model ak135, and the dashed line is for CRUST5.1. (a) P_n, (b) S_n.
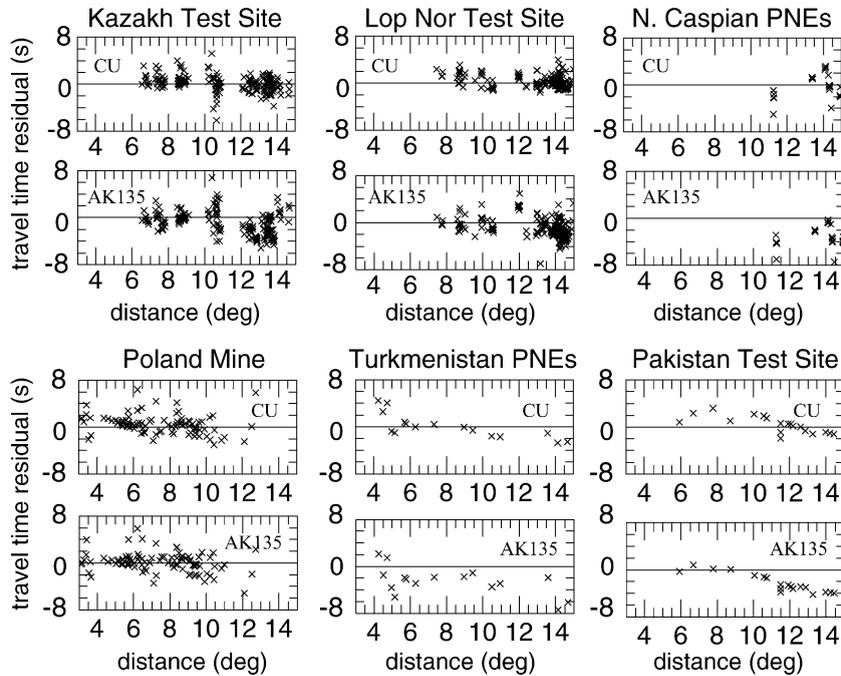
Fig. 11. Misfits to P_n and S_n measurements from selected explosions that occurred at six source locations. The upper of each pair of plots for each source location is for the CU P_n/S_n model and the lower of each pair is for the model ak135. Summary statistics are presented in Table 2.

The rms misfit is probably the best guide to the accuracy of the correction surfaces. Misfits are a strong function of epicentral distance, as Fig. 10 shows. Because the distribution of misfit is heavy-tailed and decidedly non-Gaussian, much of the overall misfit comes from bad travel time measurements that we were unsuccessful in identifying and elimi-

nating prior to inversion. The misfit statistics we report are, therefore, probably an overestimate of the error in the predicted travel times.

7. Discussion

The main purpose of this paper is to assess P_n and S_n tomography as a potential means of improving location capabilities using regional phase data alone. A full discussion of the velocity anomalies that appear in the P_n and S_n maps, therefore, is well beyond the intended scope. For greater coherence, however, we mention some of the characteristics of the estimated maps that agree with shear velocity anomalies that have emerged from surface wave dispersion studies (e.g., Shapiro et al., 2000; Villaseñor et al., 2001). It should be remembered that P_n and S_n maps are of velocities right at the top of the mantle and are mute about vertical velocity variations that are revealed by 3-D models. We will limit this discussion to Central Asia.

The old, stable cratons north of the Alpine–Himalayan orogenic belt are characterized by high

Table 2
Summary of misfits to explosion data for P_n displayed in Fig. 11

Location	# Meas.	# Stations	# Events	rms misfit (s)	
				CU P_n/S_n	ak135
Kazakh Test Site	189	18	42	1.38	2.08
Lop Nor Test Site	204	39	19	1.16	1.90
N. Caspian PNEs	22	7	6	2.10	3.72
Pakistan Test Site	19	18	2	1.43	2.72
Pol Mines	92	92	1	1.72	1.68
Turkmenistan PNEs	16	16	1	2.04	3.45
Total	542	–	–	1.68	2.71

upper-mantle P_n and S_n velocities. High velocities are also found beneath the Indian shield, the southern Tibetan Plateau, and the Tarim Basin. While high velocities in the upper mantle are usually interpreted as an indication of old, cold, thick lithospheric blocks, the structures associated with low velocity anomalies are more difficult to interpret. Large low velocity anomalies are associated with young, extensional plate boundaries, such as the Red Sea. The low velocity anomaly beneath central and northern Tibet has received a great deal of attention (see Molnar, 1988) because of its implications for the origin and mechanism for the formation of the Tibetan plateau. However, although present in the P_n and S_n maps, it is not one of the most prominent negative anomalies in magnitude or in extent. Based upon the presence of this low velocity region and other evidence (e.g., widespread Quaternary volcanism and inefficient S_n propagation), Molnar et al. (1993) proposed that the high-velocity Indian lithosphere has not been underthrusted beneath the Tibetan Plateau, and that crustal thickening has occurred by north–south shortening of the southern Eurasian crust.

One of the most prominent upper-mantle low velocity regions is located in the Middle East, extending from Turkey to Iran and western Afghanistan. This low velocity anomaly coincides with the Turkish–Iranian continental plateau, formed by the collision between the Arabian and Eurasian plates. This collision is the result of the closing of the Neo-Tethys Ocean by northward subduction of oceanic lithosphere beneath Eurasia. In Iran and western Afghanistan, the low velocity anomaly is bounded to the south by high velocities, part of the Arabian plate. This low velocity anomaly is prominent in other P_n tomography studies (e.g., Hearn and James, 1994), and is also coincident with a region of high S-wave attenuation (Kadinsky-Cade et al., 1981) and Neogene volcanism (Kazmin et al., 1986). The combination of these observations suggests a hot or perhaps partially molten uppermost mantle beneath the Turkish–Iranian Plateau. This anomalously hot upper mantle could be a remnant of the back-arc extensional regime that dominated this region from the Jurassic to the Neogene (Dercourt et al., 1986). The presence of hot, molten upper mantle weakens the lithosphere, allowing larger deformation associated with the Arabian plate–Eurasia collision. This results in the observed diffuse intraplate seismicity that extends well to the north of the plate boundary delineated by the Zagros Main Thrust. Furthermore, the buoyancy associated with hot upper mantle, combined with the buoyancy due to the deep continental roots in the region, can contribute to maintain the high topography of the plateau.

Another significant upper-mantle low velocity anomaly is centered in western Mongolia, WSW of lake Baikal. The central part of this anomaly coincides with the Hangay Dome area of central Mongolia. The Hangay Dome is characterized by recent uplift, diffuse extension and regionally upwarped topography (Cunningham, 1988). This is also a region of recent Cenozoic volcanism and high heat flow (with a maximum of approximately 80 mW/m^2). There is remarkable agreement between the shape of the velocity anomaly and the heat flow anomaly (Fig. 5a of Cunningham, 1988). This region in Mongolia has been interpreted to overlie a mantle plume or asthenospheric diapir, which is associated with rifting in Lake Baikal (Windley and Allen, 1993). Lake Baikal is located at the boundary between the Mongolian plateau and the Siberian Craton, which is consistent with the marked contrast between low and high velocities observed in our P_n and S_n maps. Irrespective of its cause, deformation due to the presence of the mantle plume or asthenospheric diapir manifests in high seismic activity in Western Mongolia, which has been the site of some of the largest intraplate earthquakes recorded during this century (i.e., 1905 and 1957).

8. Conclusions

The method for producing P_n and S_n maps with associated parametric corrections effectively summarizes the information in the large groomed ISC/NEIC data base for epicentral distances from about 3° to 15°. The P_n and S_n maps correlate well with other high resolution information about structural variations in the uppermost mantle. In particular, these maps produce relatively high resolution images of low velocity anomalies in tectonically deformed regions across the continent. These include anomalies across central and southern Asia and the Middle East that

extend along a tortuous path from Turkey in the west to Lake Baikal in the east. These anomalies are related to the closing of the Neo-Tethys Ocean and the collision of India with Asia. The uppermost mantle beneath the Pacific Rim back-arc is also very slow, presumably due to upwelling that results from back-arc spreading, as is the Red Sea rift, the Tyrrhenian Sea and other regions undergoing active extension.

The travel time correction surfaces computed from the CU P_n/S_n model appear to be robust and fit the data with low levels of bias at epicentral distances from $3°$ to $15°$. Overall rms misfits across Eurasia for P_n are ~ 1.6 s and for S_n ~ 3.2 s, are better for data subsets chosen for their quality (e.g., explosions, large magnitude events, independent information about epicenter location and/or origin time), and exhibit a strong, nearly linear distance trend. These misfits are considerably better than those produced by ak135 and CRUST5.1, although ak135 fits the P data remarkably well for a 1-D model. The correction surfaces presented here provide a reference for 3-D models to match and extend.

Although the method described here appears to produce reliable travel time correction surfaces, there are greater problems in estimating P_n and S_n reliably due to trade-offs between the estimated tomographic map and the parametric corrections. Some of these trade-offs can be ameliorated in the future if a 3-D model is used as the reference model, which will allow the horizontal ray approximation to be broken. Indeed, it is likely that our P_n model fits the data only marginally better than the 1-D model ak135 because a single distance correction is inadequate to model ray penetration into the upper mantle, which can be highly variable, as Fig. 3b indicates. Getting the vertical velocity derivative right may be more important in predicting regional travel times than mapping lateral variations. Recent models, such as those of Ekström and Dziewonski (1998), Villaseñor et al. (2001), and Shapiro et al. (2000), are providing new information about the vertical velocity gradient in the uppermost mantle which controls the depth of penetration and, hence, a large fraction of the travel time of regionally propagating phases. In addition, to extend travel time correction surfaces beyond $15°$ will require a 3-D model to predict the ray paths.

The final proof of the effectiveness of the method described here will be the relocation of ground-truth events. The agreement between observed and predicted travel times for Eurasian explosions is encouraging, but rigorous tests to determine the extent to which the correction surfaces will improve regional location capabilities define a crucial remaining hurdle.

References

Barmin, M.P., Ritzwoller, M.H., Levshin, A.L., 2001. A fast and reliable method for surface wave tomography. Pure Appl. Geophys. 158, 1351–1375.

Bijwaard, H., Spakman, W., Engdahl, E.R., 1998. Closing the gap between regional and global travel time tomography. J. Geophys. Res. 13, 30055–30078.

Cerveny, V., Psencik, I., 1988. Numerical modeling of seismic wave fields in 2-D laterally varying layered structures by the ray method. Seismological Algorithms. Academic Press, London.

Cunningham, W.D. 1988. Lithospheric controls on late Cenozoic construction of the Mongolian Altai. Tectonics 17, 891–902.

Dercourt, J., et al., 1986. Geological evolution of the Tethys belt from the Atlantic to the Pamirs since the Lias. Tectonophysics 123, 241–315.

Ekström, G., Dziewonski, A.M., 1998. The unique anisotropy of the Pacific upper mantle. Nature 394, 168–172.

Engdahl, E.R., Ritzwoller, M.H., 2001. Crust and upper mantle P- and S-wave delay times at Eurasian seismic stations. Phys. Earth Planet. Inter. 123, 205–219.

Engdahl, E.R., van der Hilst, R., Buland, R., 1998. Global teleseismic earthquake relocation with improved travel time and procedures for depth determination. Bull. Seismol. Soc. Am. 88, 722–743.

Hearn, T.M., Clayton, R.W., 1986. Lateral velocity variations in Southern California: I. Results for the upper crust from Pg waves. Bull. Seismol. Soc. Am. 76, 495–509.

Hearn, T.M., James, F.N., 1994. P_n velocities beneath continental collision zones: the Turkish–Iranian plateau. Geophys. J. Int. 117, 273–283.

Hearn, T., Beghoul, N., Barazangi, M., 1991. Tomography of the Western United States from regional arrival times. J. Geophys. Res. 96, 16369–16381.

Kadinsky-Cade, K., Barazangi, M., Oliver, J., Isacks, B., 1981. Lateral variations of high-frequency seismic wave propagation at regional distances across the Turkish and Iranian Plateaus. J. Geophys. Res. 86, 9377–9396.

Kazmin, V.G., Sbortshikov, I.M., Ricou, L.E., Zonenshain, L.P., Boulin, J., Knipper, A.L., 1986. Volcanic belts as markers of the Mesozoic–Cenozoic active margin of Eurasia. Tectonophysics 123, 123–152.

Kennett, B.L.N., Engdahl, E.R., Buland, R., 1995. Constraints on seismic velocities in the Earth from travel times. Geophys. J. Int. 122, 108–124.

Molnar, P., 1988. A review of geophysical constraints on the deep structure of the Tibetan plateau, the Himalaya and the Karakoram, and their tectonic implications. Philos. Trans. R. Soc. London, A 326, 33–88.

Molnar, P., England, P., Martinod, J., 1993. Mantle dynamics, uplift of the Tibetan Plateau, and the Indian monsoon. Rev. Geophys. 31, 357–396.

Mooney, W.D., Laske, G., Masters, G., 1998. CRUST 5.1: a global crustal model at 5 degrees by 5 degrees. J. Geophys. Res. 103, 727–748.

Myers, S.C., Schultz, C.A., 2000. Improving sparse network seismic location with Bayesian kriging and teleseismically constrained calibration events. Bull. Seismol. Soc. Am. 90, 199–211.

Shapiro, N.M., Ritzwoller, M.H., Villaseor, A., Levshin, A.L., 2000. Shear velocity structure of the Eurasian crust and uppermost mantle. Eos Trans. Am. Geophys. Union 81 (48), F861, Nov. 28.

Sultanov, D.D., Murphy, J.R., Rubinstein, Kh.D., 1999. A seismic source summary for Soviet peaceful nuclear explosions. Bull. Seismol. Soc. Am. 89, 640–647.

Villaseñor, A., Ritzwoller, M.H., Levshin, A.L., Barmin, M.P., Engdahl, E.R., Spakman, W., Trampert, J., 2001. Shear velocity structure of Central Eurasia from inversion of surface wave velocities. Phys. Earth Planet. Inter. 123, 169–184.

Windley, B.F., Allen, M.B., 1993. Evidence for a late Cenozoic mantle plume under central Asia. Geology 21, 295–298.